ADVANCED
FUNCTIONAL
MATERIALS

Supporting Information

for *Adv. Funct. Mater.*, DOI 10.1002/adfm.202302330

Bandwidth Control and Symmetry Breaking in a Mott-Hubbard Correlated Metal

Lishai Shoham, Maria Baskin, Tom Tiwald, Guy Ankonina, Myung-Geun Han, Anna Zakharova, Shaked Caspi, Shay Joseph, Yimei Zhu, Isao H. Inoue, Cinthia Piamonteze, Marcelo J. Rozenberg and Lior Kornblum**

Supporting Information

Bandwidth Control and Symmetry Breaking in a Mott-Hubbard Correlated Metal

Lishai Shoham, Maria Baskin, Tom Tiwald, Guy Ankonina, Myung-Geun Han, Anna Zakharova, Shaked Caspi, Shay Joseph, Yimei Zhu, Isao H. Inoue, Cinthia Piamonteze, Marcelo J. Rozenberg, and Lior Kornblum

1. Sample Preparation

All the substrates used here are 5×5×0.5 mm^3 supplied by CrysTec GmbH. $SrTiO_3$ (STO) substrates were TiO_2 terminated using the HF method.[1] $LaAlO_3$ (LAO) substrates were annealed in air at 1000°C for 2.5 hours. $(LaAlO3)_{0.3}(Sr_2TaAlO_6)_{0.7}$ (LSAT) substrates were annealed in air at 1300°C for 2.5 hours. SVO films for XAS and STEM analysis were grown on as-received LAO and LSAT substrates. $LaGaO_3$ (LGO) substrates were used as received.

2. Structural and Electronic Characterization

2.1. X-ray Diffraction (XRD). 2θ/ω scans around the (002) cubic/pseudocubic substrate peak were performed for all strained SVO films (Figure S1).

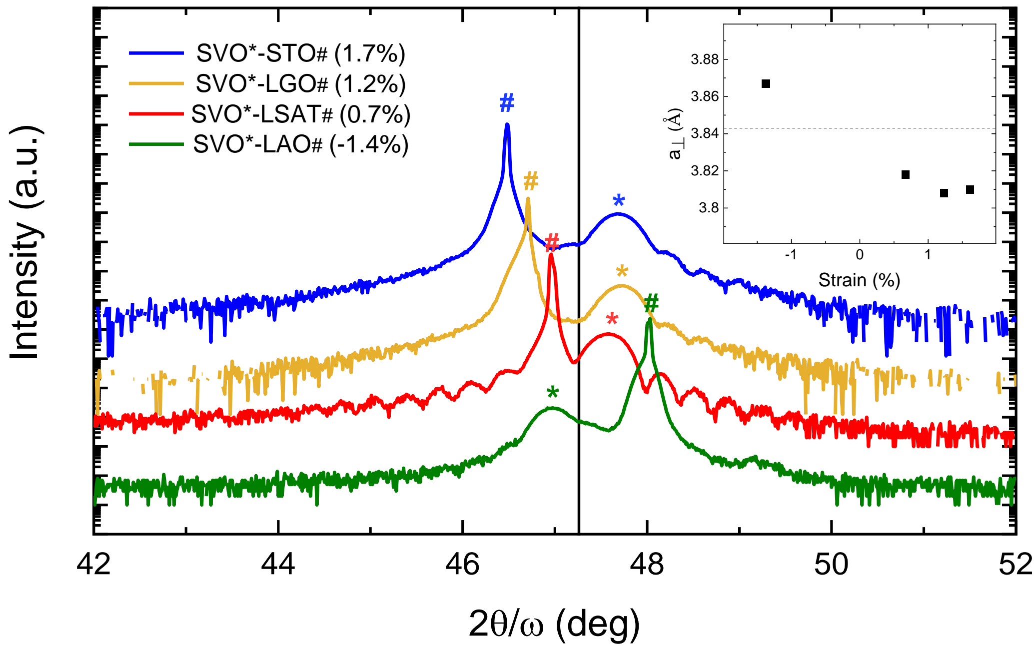

Figure S1. High resolution 2θ/ω x-ray diffraction scans around the (002) cubic/pseudocubic Bragg peak of each substrate. The shift of the SVO out-of-plane lattice parameter is illustrated in the inset, featuring the out-of-plane lattice parameter as a function of the biaxial strain.

The XRD data were fitted using GlobalFit by Rigaku, considering film thickness, film out-of-plane lattice parameter ($a_{\perp,SVO}$), and substrate lattice parameter (a_{sub}). The fit parameters are summarized in Table S1. The tetragonal distortion manifests in the elongation (shortening) of the out-of-plane lattice parameter with the increase of the compressive (tensile) strain. We note that the strained SVO film on STO substrate exhibits a deviation in this trend, as shown in the inset of Figure S1. This small deviation can be explained by the presence of a small concentration of point defects formed to accommodate the high tensile strain. Nevertheless, the transport measurement in the following section confirms that this small concentration of defects did not degrade the high quality of the film. We emphasize that the films exhibit high RRR values, meaning that the small increase in the point defect density is not expected to produce meaningful changes in the band structure.

Using the in-plane lattice parameter of the substrate (for these coherent films) and the extracted SVO out-of-plane lattice parameter, one can calculate the four inner angles of the VO_6 octahedra (designated as O1, O2, O3, and O4, see main text). The calculated angle variation indicates a ±1.5° deviation from the unstrained 90° inner angle for highly tensile and compressive strained SVO films.

Table S1. Summary of the parameters used for the XRD fitting results, and the calculated inner angles of the VO_6 oxygen octahedra.

	a_{sub} (Å)	$a_{\perp,SVO}$ (Å)	Thickness (nm)	$\Theta_{1,3}$ (deg)	$\Theta_{2,4}$ (deg)
SVO-STO	3.905	3.810	27	88.6	91.4
SVO-LGO	3.890	3.808	27	88.8	91.2
SVO-LSAT	3.868	3.818	26	89.3	90.7
SVO-LAO	3.790	3.867	29	91.2	88.8

2.2. Transport Measurements. Sheet resistance and Hall resistance were measured in the Van der Pauw geometry using a Quantum Design Physical Properties Measurement System (PPMS). The contact to the films was made using Al wire, which was directly wedged to the bare surface of the film. Sheet resistance was measured in the temperature range of 2 - 300 °K. Figure S2 illustrates the resistivity as a function of the temperature for the different strained SVO films.

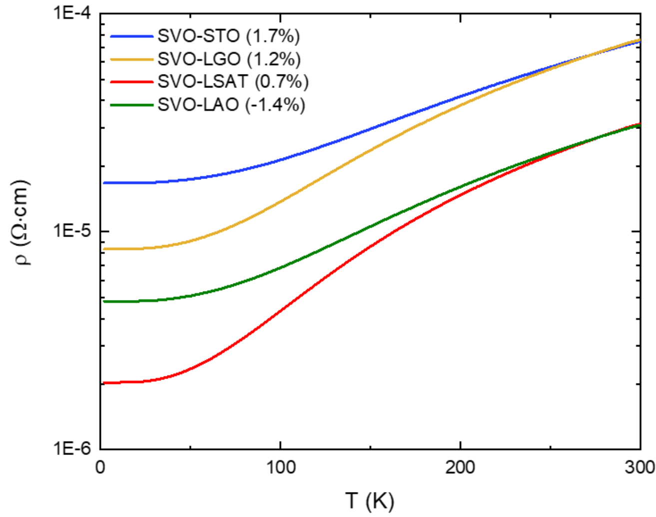

Figure S2. Temperature-dependent resistivity for the strained SVO films.

Table S2 summarizes the residual resistivity ratio (RRR), defined as ρ_{300K}/ρ_{2K}, and the room temperature conductivity of the SVO films. Hall resistance measured at room temperature between ± 4 T was used to extract the electron density and mobility. The Hall resistance was linear with magnetic field variation, presenting a negative slope indicating electrons as the carrier density.

Table S2. Summary of the transport properties as extracted from the transport measurements.

	RRR	**σ @ 300K** (10^4 S·cm^{-1})	**n @ 300K** (10^{22} cm^{-3})	**μ @ 300K** (cm^2·S^{-1}V^{-1})
SVO-STO (L303)	4.5	1.34	1.9	4.3
SVO-LGO (L298)	9.1	1.32	2.3	3.5
SVO-LSAT (L263)	15.3	3.20	2.1	9.6
SVO-LAO (L59)	6.4	3.24	1.9	10.9

3. X-ray Absorption Spectroscopy (XAS).

3.1. XAS measurements were acquired in x-ray excited optical luminescence (XEOL) mode[2] at the V $L_{2,3}$ edge for the different strained films. The x-ray was in grazing incidence, with the sample surface at 30° with the incoming x-ray beam (Figure 2b). The measurements were conducted under zero magnetic field in linear vertical and 30° to the linear horizontal polarizations with respect to the film's normal (LV and LH, respectively). The SVO-LAO and SVO-LSAT samples were measured at room temperature, while the SVO-STO sample was measured at 120 °K to increase luminescence from the STO substrate. Nevertheless, the low-temperature measurement is not expected to affect the results, as seen by the close agreement of the 120 °K to the 300 °K SVO-LSAT data (Figure 2c), which is also tensely strained. The XAS and x-ray linear dichroism (XLD) for the different strained film spectra are presented in Figure S3. We do not address the adjacent O K-edge due to the strong contribution from the substrate.

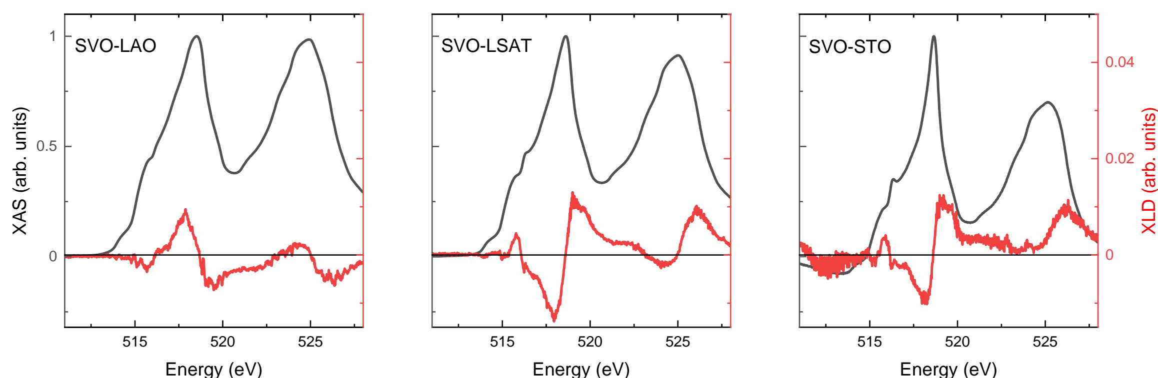

Figure S3. Normalized XAS (black) and XLD (red) at the V $L_{2,3}$ edge spectra for the strained SVO films grown on LAO, LSAT, and STO substrates measured in XEOL mode. The STO measurements were done at 120° K to increase substrate luminescence. The XAS is calculated as LH+LV, and the XLD is calculated as LH–LV.

3.2. Obtaining the absorption results from the XEOL measurement. First, we measured the sample at LH and LV polarizations at least four times each. After eliminating outliers, we separately averaged the LH and LV results and normalized them at the pre-edge to 1, as shown

in Figure S4a. Then, we used the Beer-Lambert law for linear absorption to achieve the LH and LV absorption signal. The results are presented in Figure S4b.

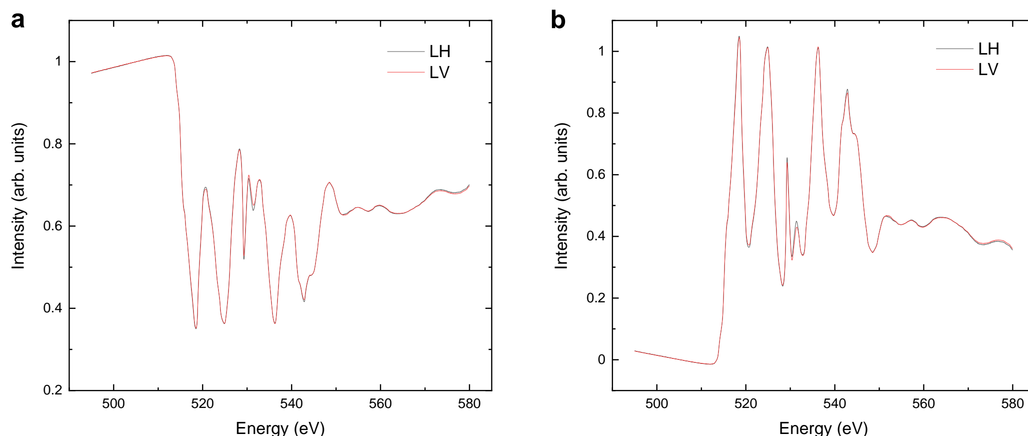

Figure S4. An example of obtaining the absorption results from the XEOL measurement of the SVO-LAO sample. a) Averaged XEOL intensity as recorded for LH (black) and LV (red). The data were normalized to 1 at the pre-edge. b) The calculated absorption for LH (black) and LV (red) using Beer-Lambert law for linear absorption.

3.3. Normalizing the XAS and XLD results: we calculated the XAS to be LH+LV and the XLD to be LH-LV. For the XAS, we subtracted a linear background fitted to the pre-edge and normalized it to 1 at L_3 maximum. The XLD was normalized by the same factor used to normalize the XAS (no background was subtracted from the XLD).

4. Spectroscopic Ellipsometry (SE).

4.1. SE measurements. All strained SVO films and bare substrates were measured using *ex-situ* SE at room temperature. The ellipsometry spectra (in ψ, Δ) were collected using focusing probes to reduce the beam diameter to approximately 300 μm, which allowed the illuminated area to easily fit on the relatively small samples. No other sample preparation was necessary.

4.2. SE modeling. The complex dielectric function ($\varepsilon = \varepsilon_1 + i\varepsilon_2$), presented in Figure S5, was obtained by fitting the ellipsometry spectra collected over the near IR to UV range. The spectra were fitted to a model consisting of a semi-infinite substrate / SVO film using

CompleteEASE® software (J. A. Woollam Co.). For some of the samples, an additional surface roughness layer was added. The goodness of the fit is quantified by using the Root Mean Squared Error.[3]

The substrates' dielectric functions were determined from separate measurements of the bare substrates. The LGO substrate is anisotropic; therefore, it was modeled with a uniaxial dielectric tensor. During measurement, this sample was oriented such that the optic axis was parallel to the plane of incidence, meaning there is no significant p-to-s conversion, and the standard ellipsometry measurement provides accurate results.

The films' layer was fitted using a Kramers-Kronig consistent B-spline function and a fixed thickness extracted from x-ray reflectivity (XRR) measurements (when the surface roughness layer was added, the total thickness was fixed). Then, the parameterization of the layer ε_2 was done using the following five oscillators:[4]

I. Drude peak with fixed carrier density (taken from Table S2).
II. Lorentz function at the U/2 energy (~1.8 eV).
III. Tauc-Lorentz function at the CT(t_{2g}) energy (~3.2 eV).
IV. Lorentz function at the CT(e_g) energy (~5.5 eV).
V. Additional Lorentz function at the energy ~4.5 eV.

The contribution from the U excitation was neglected, as elaborated in the main text.

Each of these five complex functions is Kramers-Kronig consistent, meaning that the ε_1 of the layer has the correct line shape within a constant offset, which is determined by fitting a constant ε_∞. For SVO-LSAT and SVO-STO, an additional surface roughness layer was added.

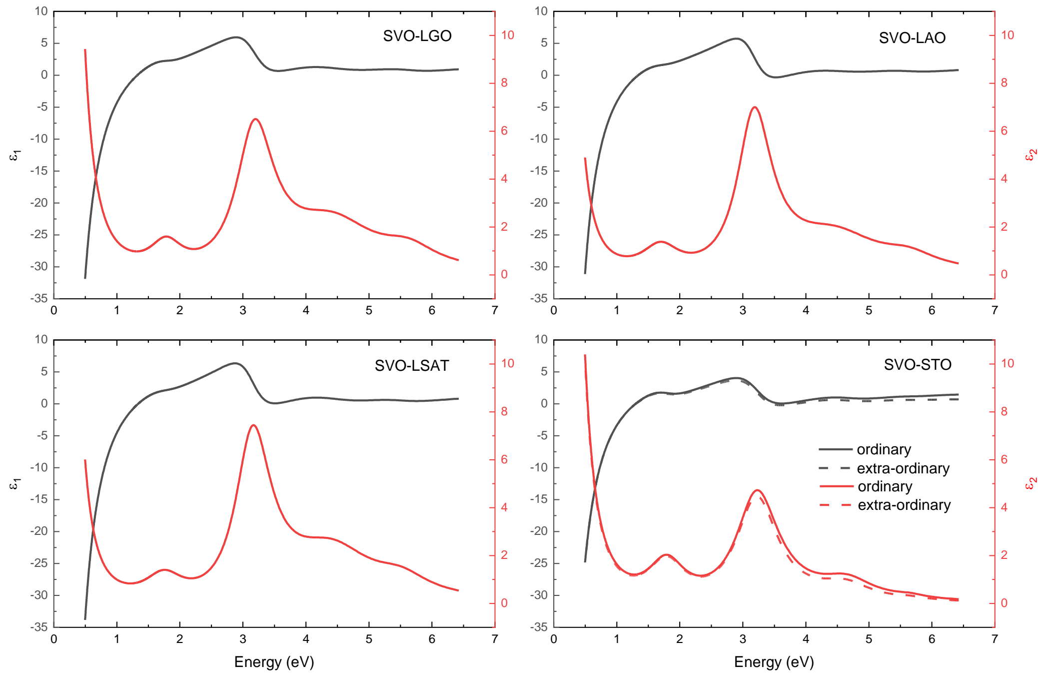

Figure S5. Real and imaginary dielectric functions spectra (black and red, respectively) of strained SVO films grown on LGO, LAO, LSAT, and STO substrates. The spectra were extracted from room-temperature spectroscopic ellipsometry measurements. For SVO-STO we used a uniaxial model, as elaborated below.

We found that using a uniaxial model (n_x,$n_y \neq n_z$) significantly improves the fit for the SVO-STO sample. In this model, the in-plane dielectric function (ordinary) is determined as elaborated above, whereas the out-of-plane dielectric function (extra-ordinary) is modeled by adding a small difference value to the in-plane index n(λ). The SVO-STO optical conductivity in Figure 3a is therefore based on the in-plane component. We note that the epitaxial strain is expected to create an optical anisotropy between the in-plane and out-of-plane dielectric functions. However, the sensitivity to this change is negligible due to the low thickness of the films (compared to the measurement wavelength). As it appears, there is a small sensitivity under high tensile strain (SVO-STO). While the anisotropic model improves the goodness of the fit, the fit result and trend are unchanged whether an isotropic or an anisotropic model is used.

We further considered the effect of the near-surface region (NSR) observed on SVO films[5,6] on the reliability of the model. To that end, we modeled the SVO layer as elaborated before (4.2 SE modeling) and added an independent B-spline surface layer with a fixed thickness of 4 nm.[5] The total thickness (layer + NSR) was fixed to the thickness measured via XRR. As a result, the additional surface layer did not improve the fit substantially, and the layers‘ optical constants were similar to the previous models. Therefore, we conclude that there is minor sensitivity to the presence of the surface region.

4.3. The optical conductivity was calculated using the relation:

$$\sigma(\omega) = -i\varepsilon_0[\varepsilon(\omega) - 1]\omega \quad (1)$$

where ε_0 is the vacuum dielectric constant, ε is the complex dielectric function (see Figure S5), and ω is the frequency. The energy-dependent real part of the optical conductivity, as calculated for the full measured spectrum range, is presented in Figure S6. For metals, optical conductivity consists of intraband transitions of free electrons within the conduction band (Drude), and interband transitions of bound electrons from lower energy bands to the unoccupied part of the conduction band. An example of the latter is the transition from the occupied O 2*p* band to the unoccupied TM-3*d* band, named charge transfer (CT).

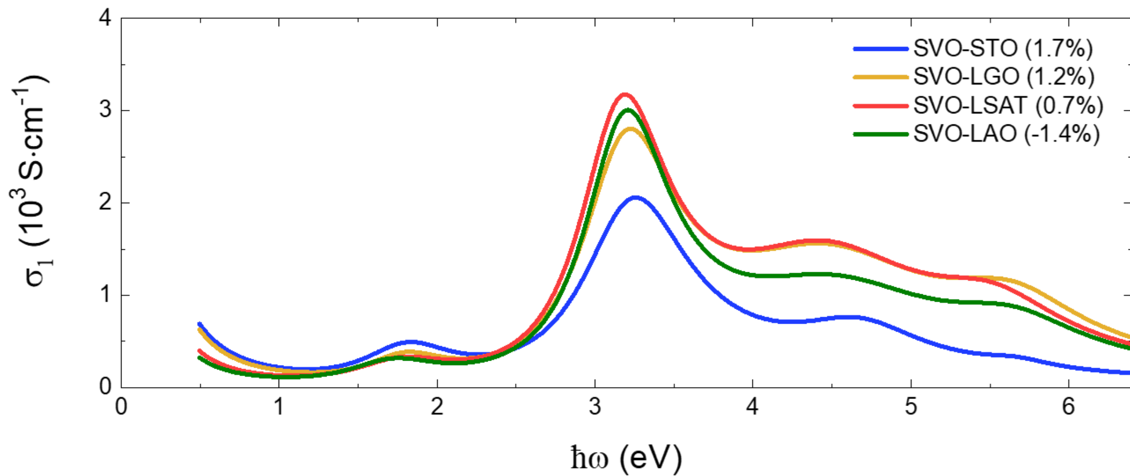

Figure S6. Optical conductivity of SVO under tensile and compressive strain. Peaks at energies above 4.2 eV are ascribed to additional excitations from the broad O 2*p* states to the unoccupied V states (e.g., V-3*d* e_g states).[4]

The reduced optical conductivity (Figure 3b) was calculated from the summation of oscillators I and II (4.2 SE modeling), representing the Drude peak and U/2 excitation. Thus, the reduced optical conductivity is composed only of the V-3*d* intraband excitations.

4.4. The Drude model. From the modeling of the Drude peak using the CompleteEASE software, we can extract the optical mobility (Figure S7a), optical dc conductivity (Figure S7b), and effective mass (Figure S7c). The similar values for μ and σ_{dc} extracted from the optical and transport measurements attest to the reliability of the optical analysis. The effective mass increase going from compressive to tensile agrees with our theoretical expectations that the increase in V-O bond length increases the correlation strength.

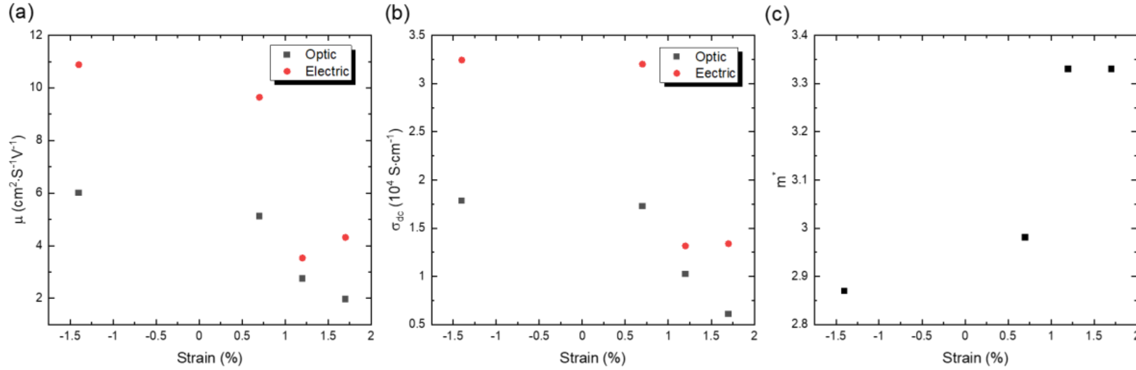

Figure S7. SVO mobility a) and dc conductivity b) as extrapolated from the optical measurements (black) or electrical measurements (red), respectively. c) The SVO effective mass was also extrapolated from the optical measurements. The data was acquired at room temperature.

Using the optical values, the Drude peak can be extrapolated via the relation (Figure S8):[7]

$$\varepsilon_{Drude}(\omega) = \frac{-q^2 N\mu}{\varepsilon_0(\mu m^* m_e \omega^2 + iq\omega)} \tag{2}$$

where ω and ε_0 are the frequency and vacuum dielectric constants, respectively. N is the carrier density, and q, m_e, m^*, and μ are the electron charge, rest mass, effective mass, and mobility, respectively. Extrapolation of the measurement to $\omega \rightarrow 0$ is done using the measured carrier densities (Eq. 2, Table S2).

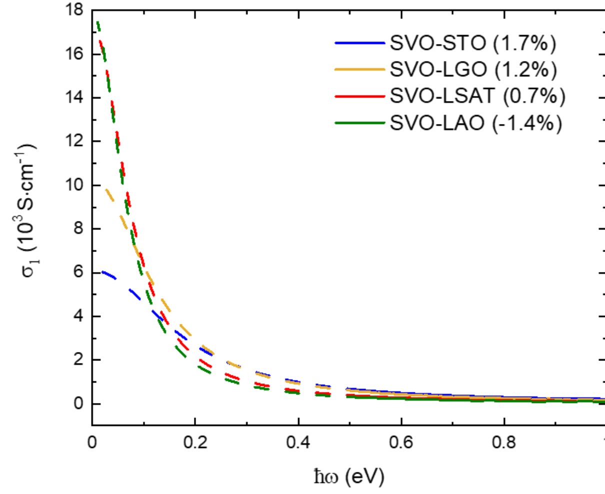

Figure S8. The Drude peak optical conductivity in the measured range (solid) and as extrapolated using equation 2 (dashed).

4.5. Effective number of electrons. By considering the sum rule of the conductivity spectra, we can estimate the effective number of free carriers (N_{eff}) defined as:

$$N_{eff} = \frac{2m}{\pi e^2 V} \int_0^{\omega} \sigma(\omega')d\omega' \quad (3)$$

Here, m is taken as m_0, the free electron mass, V is the number of vanadium atoms per unit volume, and ω is the frequency. The effective number of free carriers is proportional to the number of electrons involved in the optical excitations up to frequency ω. $N_{eff}(\omega)$ for the strained SVO films is presented in Figure S9.

Theoretically, one free electron is expected per SVO unit cell. However, we have assumed that the electron mass equals the free carrier mass ($m = m_0$), whereas it is expected to be higher ($m > m_0$) due to the electron correlation. When we consider the extrapolated effective mass (~3.0, as extrapolated from the SE. See Figure S7c), N_{eff} equals one at about ~1 eV. This result agrees with our understanding that the majority of the V 3*d* single-particle spectral weight is within the quasiparticle peak.

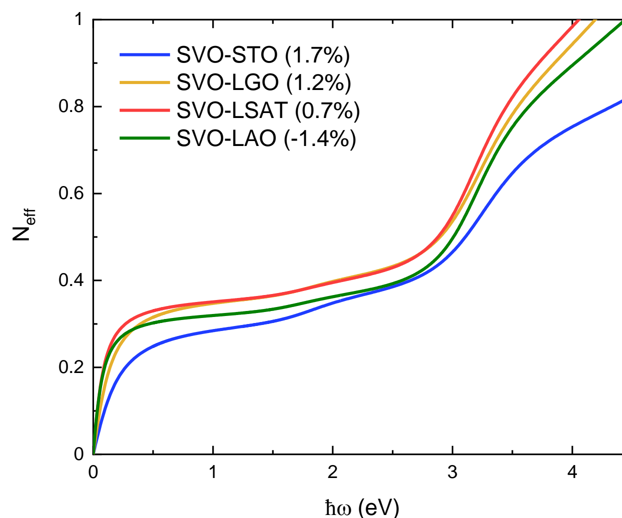

Figure S9. Effective electron number per vanadium atom for the different strained SVO films.

5. Scanning Transmission Electron Microscopy.

5.1. Tensile Strain: SVO-LSAT Sample.

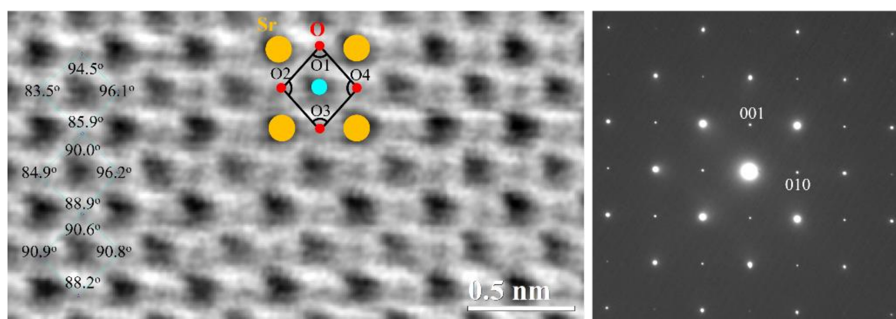

Figure S10. Cross-section high-resolution scanning transmission electron microscopy (STEM) micrographs of a tensile strained SVO film on LSAT substrate imaged with annular bright-field (ABF) along the [100] axis. It shows the oxygen octahedra inner angle measurements and selected area electron diffraction patterns from the SVO and LSAT substrate. The measured angles are shown on the selected octahedra. The measurements show that the average horizontal angles (O2 and O4) are 90.4 ± 4.9° while the vertical angles (O1 and O3) are 93.0 ± 2.6°.

References

[1] G. Koster, B. L. Kropman, G. J. H. M. Rijnders, D. H. A. Blank, H. Rogalla, *Appl. Phys. Lett.* **1998**, *73*, 2920.

[2] C. Piamonteze, Y. W. Windsor, S. R. V. Avula, E. Kirkc, U. Staub, *J. Synchrotron Radiat.* **2020**, *27*, 1289.

[3] J. N. Hilfiker, N. Singh, T. Tiwald, D. Convey, S. M. Smith, J. H. Baker, H. G. Tompkins, *Thin Solid Films* **2008**, *516*, 7979.

[4] R. J. O. Mossanek, M. Abbate, P. T. Fonseca, A. Fujimori, H. Eisaki, S. Uchida, Y. Tokura, *Phys. Rev. B* **2009**, *80*, 195107.

[5] S. Caspi, L. Shoham, M. Baskin, K. Weinfeld, C. Piamonteze, K. A. Stoerzinger, L. Kornblum, *J. Vac. Sci. Technol. A* **2022**, *40*, 013208.

[6] J. Gabel, M. Pickem, P. Scheiderer, L. Dudy, B. Leikert, M. Fuchs, M. Stübinger, M. Schmitt, J. Küspert, G. Sangiovanni, J. M. Tomczak, K. Held, T. L. Lee, R. Claessen, M. Sing, *Adv. Electron. Mater.* **2022**, *8*, 2101006.

[7] T. E. Tiwald, D. W. Thompson, J. A. Woollam, W. Paulson, R. Hance, *Thin Solid Films* **1998**, *313–314*, 661.